Flextegrity simple cubic lattices

*Original*
Flextegrity simple cubic lattices / Boni, C; Royer-Carfagni, G. - In: PROCEEDINGS OF THE ROYAL SOCIETY OF LONDON. SERIES A. - ISSN 1364-5021. - 479:2270(2023). [10.1098/rspa.2022.0637]

*Publisher:*
ROYAL SOC

*Published*
DOI:10.1098/rspa.2022.0637

# Flextegrity simple cubic lattices

Claudio BONI[a], Gianni ROYER-CARFAGNI[a,b,*]

[a] *Department of Engineering and Architecture, University of Parma, Parco Area delle Scienze 181/A, I-43100 Parma, Italy*

[b] *Construction Technologies Institute - Italian National Research Council (ITC-CNR), Via Lombardia 49, I-20098 San Giuliano Milanese, Milano, Italy*

## Abstract

Flextegrity lattices are spatial grids composed of stiff segments kept in contact by compliant pre-tensioned tendons. The kinematic skeleton is sensible to the orientation of the segments, since their relative rotation produces the straining of the tendons to an amount that depends upon the angle of rotation and the shape of the pitch surfaces of the contact joints: these dictate the constitutive properties of the lattice in response to external actions. Two- and three-dimensional lattices are investigated, in which the contact pitch surfaces, obtained with axial-symmetric toothed conjugate profiles, mimic the kinematics of spheres, centered are at the nodes of a simple cubic lattice, in pure rolling motion. The allowed mechanisms are discussed under infinitesimal deformation, to recognize possible eigenstress states in the lattice. The response under finite deformations is worked out for two-dimensional lattices under symmetric and asymmetric loading. The theoretical predictions are compared with experimental results on 3D-printed physical models. Possible extensions are discussed for lattices with segments of varying size, different arrangements, and multi-stable contact joints. The flextegrity microstructure can represent a mesoscopic model for homogenous crystals composed of non-pointwise molecules, but it could actually be manufactured in metamaterials with peculiar properties.

---

*Corresponding author

*Email addresses:* `claudio.boni@unipr.it` (Claudio BONI), `gianni.royer@unipr.it` (Gianni ROYER-CARFAGNI)

*December 20, 2022*

*Keywords:*
flextegrity (flexural tensegrity), lattice solid model, segmental grids, segmental joints, structural mechanics.

---

## 1. Introduction

In the remarkable *Robert Boyle Lecture*, delivered before the Oxford University Junior Scientific Club on May 16th 1893 (reprinted in Appendix H of the Baltimore Lectures [1]), Sir William Thomson, 1st Baron Kelvin, while discussing the "The Molecular Tactics of a Crystal", presents his insightful view of the constitution of matter. Every crystal is a homogenous assemblage of small bodies (molecules), *all equal, similar and in precisely similar attitudes*. Each member of the assemblage may be regarded as a single point but this is a drastic approximation. One should consider that each member is a group of points, or a globe, or a cube, or another geometrical (possibly chiral) figure, in reciprocal contact on a set of points, or lines, or surfaces. The solids may be perfectly smooth and frictionless, or in frictional contact, or connected by forces operating at a distance. The coherent assemblage constitutes a kinematic frame or skeleton for an elastic solid of very peculiar properties: change of shape of the whole can only take place in virtue of rotation of the constituent members, relative to each other. An interesting problem is represented by supposing any mutual forces, such as may be produced by springs, to act between the solid molecules, and investigating configurations of equilibrium on the supposition of frictionless contacts. The solution of it is that the potential energy of the springs must be stationary for equilibrium, and a minimum for stable equilibrium, but the constitutive properties are dictated, besides the nature of intermolecular forces, by pure geometric consideration of kinematic compatibility. This interpretation of the macroscopic properties of a crystal, defined by the geometry of the constituent members, the nature of their contact, and the type of intermolecular forces, is *mesoscopic* [2], being halfway between the *microscopic* level of detail, where particles can be taken into account through quantum physics, and the *macroscopic* level of continuum mechanics.

Mesoscopic models are usually discrete lattices of points, where lumped masses interact through elastic forces that depend on mutual distance, schematized as extensional spring linkages [3]. Going beyond the simplest linear elastic response, these can be characterized by nonlinear laws and multi-stable

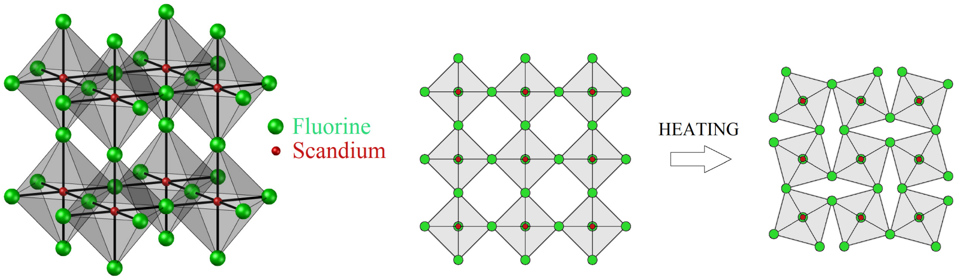

(a) (b)

Figure 1: Scandium fluoride lattice: (a) schematics of the crystalline lattice with indication of octahedral meso-structures; (b) octahedral rotation at increasing temperature, causing bulk contraction.

equilibrium states [4, 5], in order to achieve complex stress-strain paths at the macroscopic level. Micropolar bodies can be represented by grid frameworks, where meso-particles are linked by beam-like connectors [6, 7]. The field of application of such models is very wide, ranging from the analysis of propagating acoustic waves in elastic media [8] to the modeling of vibrations of tensioned membranes [9], from fluid-structure interaction [10] to the reproduction of facial movements [11]. A major limitation in models of this kind is that the points are seen as irrotational entities; instead, there are materials composed by the aggregation of subelements (meso-particles) whose relative rotations cannot be disregarded. An illustrative example is that of scandium fluoride ($ScF_3$) whose microstructure, shown in Figure 1(a), is represented by octahedral-shaped meso-particles. These can relatively rotate when heating is provided [12], causing a reduction of volume according to the mechanism of Figure 1(b), responsible of a negative thermal-expansion coefficient. For such a material the basic mesoscopic element cannot be point, but a member with geometric shape, whose configuration is defined by its rotation.

In order to account for "rotational" effects and, specifically, torsional vibrations of the lattice members, it is common to conceive mass-spring models where additional eccentric springs connect the body of two adjacent meso-constituents, with anchoring points different from their centroids [2]. This approach is followed for the representation of chiral metamaterials, when the connectors are not symmetrically placed [13, 14]. Another class is represented by lattice solid models [15], consisting of non-pointwise particles linked by bond of various nature. This "discrete element modeling" of matter can interpret macroscopic mechanical properties of structured materials [16].

Here, we present a new conceptual structure for two- and three-dimensional lattices with non-chiral structure. These will be referred to as *flextegrity lattices*[1], because they represent the extension to the spatial case of *flexural tensegrity*. This is a structural principle first proposed in [19] for beams composed as a chain of pierced segments in unilateral contact, tied together by a *tensioned* (prestressing) cable providing *integrity* and *flexural* capacity.

The key property is that the contact surfaces between adjacent segments are curved in such a way that each contact joint opens up as a consequence of the relative segmental rotation, making the tendon elongate. The shape of the contact profiles and the stiffness and pre-tension of the tendon determine the strain energy of the system. The original one-dimensional concept of flexural tensegrity has been declined in many ways. Different contact shapes provide diverse constitutive properties [19]. The continuum limit, when the number of segments goes to infinity and their length to zero, is a particular type of Euler's elastica [20], with nonlinear and nonlocal bending stiffness. Enlarging the cavities of the segments modifies the energy landscape, making it non-convex in type [21], and possibly permitting the activation of sequential snap-through instabilities in response to localized perturbations [22].

When passing to spatial lattices, the major difficulty certainly consists in the design of the contact joints. Here, we detail the simplest case in which the kinematics of the segments mimics that of balls of radius $R$ in pure rolling contact (no-sliding), with their centers at the points of a simple cubic lattice of size $2R$. The segments are held together by straight tendons, following the direction of the primitive vectors of the lattice. The skeletal structure constrains the kinematics; the energy of the system results from the straining of the tendons consequent to the relative rotation of the segments.

Flextegrity lattices could define mesoscopic models for crystals. Remarkable are the similarities with the nanostructure of fullerite, composed of fullerene balls as indicated in Figure 2(a). The spherical structure of fullerene, with a diameter of $0.714\,\mathrm{nm}$ [2], is shown in Figure 2(b) with reference to Buckminsterfullerene $\mathrm{C}_{60}$ [23] with 60 carbon atoms. It recalls

---

[1] We decided to shorten "flexural-tensegrity lattice" to "flextegrity lattice" because we have experienced that the term "tensegrity" is too reminiscent of the word coined by Füller [17, 18] as a portmanteau of *tensile integrity*, to denote assemblies of ties tensioned against a few floating struts. This has caused some terminological confusion, because classical tensegrities have no relevance to the flexural properties analyzed here.

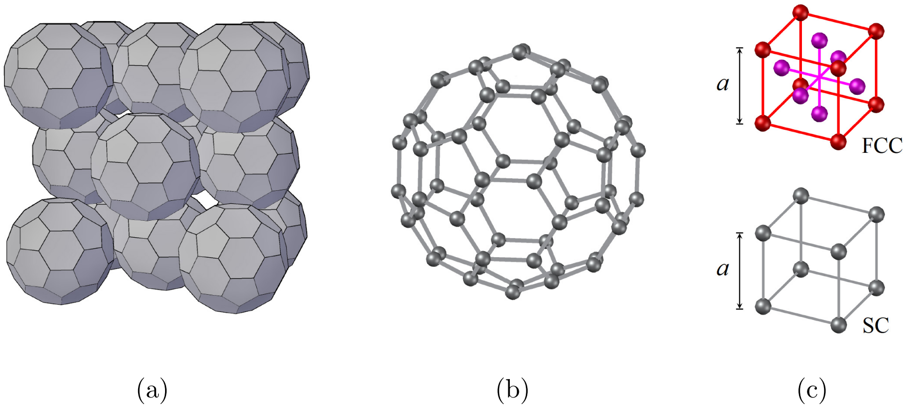

(a) (b) (c)

Figure 2: Fullerite and fullerene crystalline structure. (a) Basic unit of fullerite lattice at room temperature, composed of members of (b) Buckminsterfullerene (type of fullerene with formula $C_{60}$). (c) Face-centered cubic (FCC) lattice for fullerite at room temperature, and simple cubic (SC) lattice for fullerite at lower temperature.

the same tessellation (hexagons and pentagons) of soccerballs, as well as the geometric structure of the geodesic domes theorized by Buckminster Füller (hence, the name Fullerene). The fullerite crystal at room temperature [24] is a face-centered cubic (FCC) lattice with parameter $a = 1.417\,\mathrm{nm}$ (Figure 2(c)), whose points are the centers of fullerene balls. At 260 K a phase transition begins, in which the mesoscopic arrangement is transformed from FCC to simple cubic (SC) lattice (Figure 2(c)). At room temperature fullerenes are free to rotate [24] independently one another at high frequency, but at lower temperature (SC lattice, below 200 K) the mobility is restrained: the orientation of the rotation axis is always the same and the molecules perform torsional vibrations, relatively rotating with jump-like movement [2] only when a certain energy barrier is occasionally overcome.

The analogy with crystalline lattices is kinematical, because flextegrity assemblies are characterized by the relative rotation of the segments as main deformation mechanism. Although the model accounts for relative rotations of sub-constituents with finite amplitude, not for their spin, it appears suitable for those materials in which torsional vibrations play a major role. The flextegrity lattice can also inspire metamaterial with tailor properties, depending on the shape of the contact surface and the mutual spatial placement of segments. Anyway, this study is a field of research *per se*, as it represents the nontrivial spatial extension of the structural principle introduced in [19].

## 2. The model

After recalling the concept of flextegrity for one-dimensional beams, its extension to three-dimensional geometries is presented.

### *2.1. Contact joints in flextegrity segmental beams*

The primitive concept of “flexural tensegrity” [19], here shortened in “flextegrity”, refers to segmental beams. The segments are pierced in the centroidal axis and they are held together by a pre-tensioned cable (tendon) passing through the holes and anchored at the end sections. Figure 3(a) is a schematic representation of the contact joint between any two consecutive segments; the contact surfaces are shaped according to toothed profiles, as in gears, to prevent sliding. The corresponding pitch lines are arcs of circle, which are drawn in red in Figure 3(a), while the passing-through tendon is represented by the green line. Under tensile forces, when the prestress induced by the tendon is overcome, the segments detach as indicated in Figure 3(b), so that the axial stiffness is due to the elasticity of the tendon. When subjected to shear loading, as in Figure 3(c), the deformation depends on the elastic compliance of the teeth. Under compression, the contact surfaces flatten due to Hertzian contact, as per Figure 3(d). The response to pure bending is led by the relative rotation of the segments along the design pitch lines, as shown in Figure 3(e): the tendon is strained due to the opening of the joint, while the segments are subjected to localized compressions at the contact point.

If the tendon is compliant, as in most practical applications, the bulk deformation of the segments can be neglected. In this case, the joint is almost

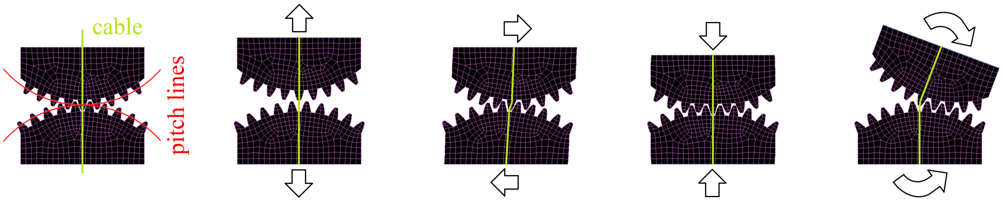

(a) (b) (c) (d) (e)

Figure 3: Schematics of a flextegrity joint for beam-like structures, with toothed contact profiles corresponding to circular pitch lines. (a) Reference state, with indication of the cable (green line) and the pitch lines (in red); (b) detachment of segments under tensile forces; (c) deformation of teeth and segments under shear forces; (d) deformation of segments under compression loading; (e) relative rotation of segments under bending.

rigid under shear and compression (Figures 3(c) and 3(d)). The deformation due to tensile actions (Figure 3(b)) depends on the cable prestress and its axial stiffness. Under bending (Figure 3(e)), the response is governed by the straining of the cable, which is forced to elongate by the relative rotation of the segments, while the segments remain practically undeformed.

To detail the response under bending, Figure 4(a) illustrates the paradigmatic case of circular pitch lines of radius $R$. Let $N_0$ denote the initial prestress of the cable and $K$ its effective axial stiffness. When the consecutive segments $i$ and $i+1$ are relatively rotated by the quantity $\Delta\varphi_i$, the segments follow pure rolling along the pitch lines. The pitch point moves from the cable exit point to the position $P_i$, while the cable elongates of the quantity $\Lambda_i$. The distance between the portion of the cable that becomes exposed (of length $\Lambda_i$, between the two exit points from the segments) and the pitch point $P_i$, indicated as $a_i$ in Figure 4(a), is the internal lever arm. Hence, the internal bending moment $M_i$ at the joint, computed with respect to the pitch point, can be written as $M_i = N\,a_i$, where $N$ is the tension force in the cable. If the cable can frictionless slide inside the holes and it is anchored at the end-segments only, its elongation is the sum of all the joint elongations $\Lambda_i$. For a segmental beam composed of $n$ segments and $n-1$ contact joints, the total elongation of the cable is $\Lambda = \sum_{i=1}^{n-1} \Lambda_i$, while the axial force in the cable passes from the initial pre-tension $N_0$ at rest, to the value $N = N_0 + K\,\Lambda$ after bending.

The amount of cable elongation $\Lambda_i$ under bending and the internal lever arm $a_i$, are only dictated by the shape of the pitch profiles and the amount of relative rotation. For the case of circular pitch profiles, one has

$$\Lambda_i = 2R\Big(1 - \cos\frac{\Delta\varphi_i}{2}\Big)\,, \tag{2.1a}$$

$$a_i = R\sin\frac{\Delta\varphi_i}{2}\,. \tag{2.1b}$$

Observe that $\Lambda_i$ and $a_i$ are correlated by pure kinematics, since it is possible to demonstrate [19, 21], for any given convex shape of the pitch profiles, that $a_i = \mathrm{d}\Lambda_i/\mathrm{d}\Delta\varphi_i$. This relationship is confirmed, for the case of circular pitch profiles, by direct differentiation of (2.1a).

In order to analyze the mobility of the joint, one can again refer to the case of circular pitch lines as per Figure 4(a). Assume, for simplicity, that

$2R$ is the segmental length along the longitudinal centroidal axis, so that the reference point $C_{i+1}$ corresponds to the segment centroid. If the segments $i$ and $i+1$ relatively rotate of $\Delta\varphi_i$ , $C_{i+1}$ moves to the new position $C'_{i+1}$ . With respect to the reference frame shown in Figure 4(a), define the displacements

$$\Delta x_i = -2R\left(1 - \cos\frac{\Delta\varphi_i}{2}\right), \quad \text{and} \quad \Delta y_i = 2R\sin\frac{\Delta\varphi_i}{2}, \tag{2.2}$$

while the lever arm and the cable elongation are defined by (2.1). If $\Delta\varphi_i$ is an infinitesimal quantity (small deflections and rotations), one can write

$$\Delta x_i \simeq 0\,, \quad \Delta y_i \simeq R\,\Delta\varphi_i\,, \quad \Lambda_i \simeq 0\,, \quad \text{and} \quad a_i \simeq R\,\Delta\varphi_i/2\,, \tag{2.3}$$

while the internal bending moment reads $M_i = N\,a_i \simeq N_0 R\,\Delta\varphi_i/2$ .

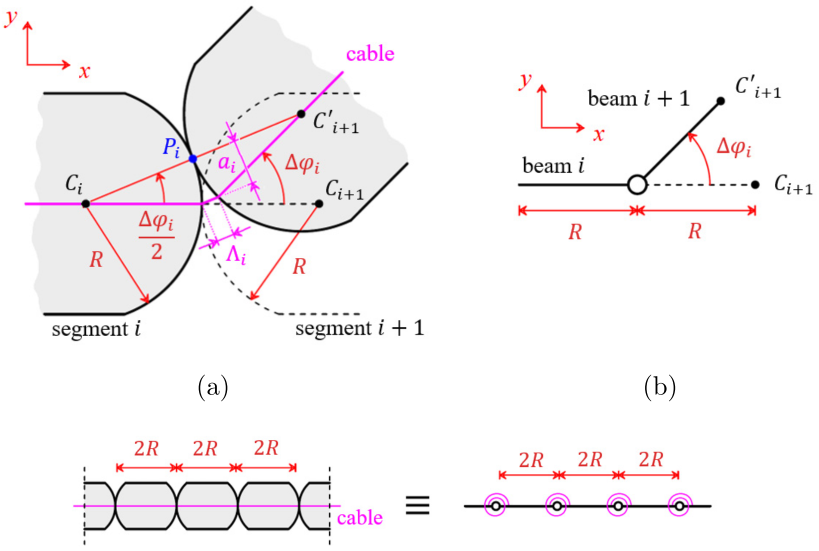

(a) (b)

(c)

Figure 4: Schematics of a flextegrity joint and comparison with a pin joint. (a) Flextegrity joint between segments $i$ and $i+1$, with indication of the cable elongation $\Lambda_i$ and the lever arm $a_i$ : the reference point $C_{i+1}$ moves to $C'_{i+1}$ after a relative rotation of $\Delta\varphi_i$ . (b) Pin joint, connecting beam segments $i$ and $i+1$. (c) Equivalence between the flextegrity and the spring-hinged joint under the hypothesis of small deflections.

It should be observed that the kinematics is equivalent to that of a pin hinge, indicated in Figure 4(b), only in the case of infinitesimal rotations. In fact, for finite deformations, one would find $\Delta x_i = -R(1 - \cos \Delta\varphi_i)$ and $\Delta y_i = R \sin \Delta\varphi_i$ . There is therefore a substantial difference, associated with rolling motion of the segments along the pitch profiles.

Under the hypothesis of small rotations, the flextegrity joint is equivalent to a spring hinge with constant $k_\varphi = N_0\, R\, /\, 2$. In this case, the flextegrity assembly can be modeled as a chain of segments connected by 3D spring hinges, representing the spatial extension of the 2D case of Figure 4(c). In the limit in which the prestressing force in the cable vanishes ($N_0 \to 0^+$), the flextegrity joint is equivalent to a spherical hinge. However, in this condition, the detachment of the segments under tensile forces (Figure 3(b)), is not prevented.

### *2.2. The spatial assembly*

The flextegrity grid considered here mimics the kinematic skeleton of spheres of radius $R$ in pure rolling contact (no sliding) along their surfaces. Figure 5(a) refers to a SC lattice, where the sphere centers are placed at the vertices of the cubic unit cell of size $2R$. The spheres are kept in contact by three orthogonal families of straight prestressing cables (tendons) passing through holes drilled in them, as indicated in Figure 5(b). If the cables are compliant, one can neglect the deformation of the spheres and regard them as rigid bodies. Clearly, the resulting assembly is incompressible under uniformly distributed positive (inwards) pressures applied to the boundary; under negative (outward) pressures, it will not be deformed as long as the prestress from the tendons is not exceeded.

The spheres are supposed to be in pure rolling contact: this is a strong kinematic constraint that limits their mobility. Consider, for example, one layer of the assembly, indicated in Figure 5(c). If one sphere rotates in the clockwise direction, the condition of no-sliding requires that the neighboring ones rotate counter-clockwise. Remarkably, the rotation of one sphere affects the rotations of *all* the other spheres of the layer, which are forced to rotate of the same angle (in absolute value), alternatively clockwise or counter-clockwise. This is a *nonlocal* interaction that affects instantaneously the whole layer where the sphere, which is first rotated, is placed. Another noteworthy property is that shear-like distortion of the lattice, of the type represented in Figure 5(d), is not allowed, because this would involve the

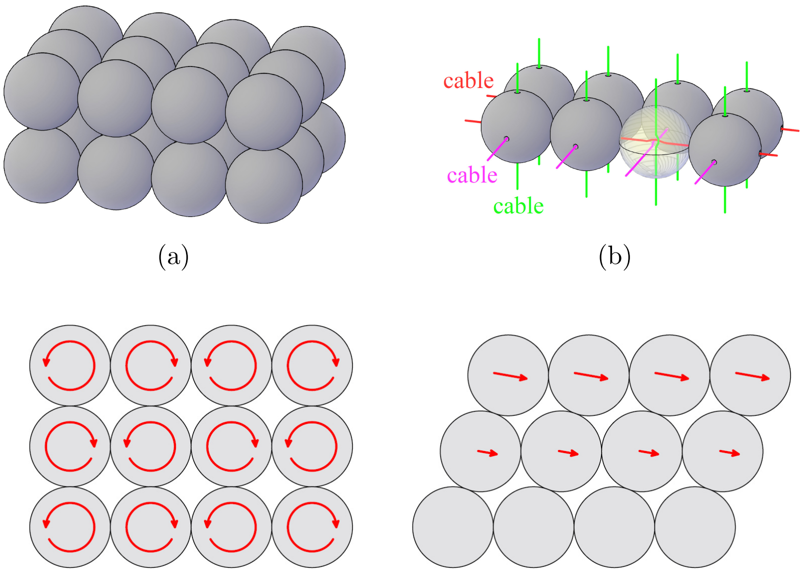

(a) (b)

(c) (d)

Figure 5: Spheres in contact: (a) assembly of spheres in the SC lattice and (b) detail of one layer with indication of the three families of prestressing tendons. The spheres are in pure rolling contact: (c) allowed relative rotation, and (d) forbidden shear-like deformation.

reciprocal slipping of some of the surfaces in contact. Moderate shear distortion would be permitted only by the deformation of the material of which the spheres are made.

Here, we consider a particular kinematic constraint, represented in Figure 6(a), where the relative motion between any two "rigid" spheres $i$ and $j$ is fully described by the torsion angle $\Delta\psi_{ij}$ , the longitude angle $\Delta\vartheta_{ij}$ , and the angle $\Delta\varphi_{ij}$ corresponding to pure rolling along the meridian. In the reference (undistorted) state, in which the tendons are straight, the center of the spheres, $C_i$ and $C_j$ , and the cable exit points, $E'_{ij}$ and $E''_{ij}$ , which coincides in the same point $E_{ij}$ , are aligned on a straight line. Starting from this configuration, the sphere $j$ can *freely* rotate (without straining the tendon) with respect to the adjacent sphere $i$ of the angle $\Delta\psi_{ij}$ around the axis passing through $C_i$ , $C_j$ and $E_{ij}$ (the cable cannot provide any stiffness against twist). Then, the spheres can pure roll one another along that meridian (with the "North" pole in $E_{ij}$) identified by the longitude angle $\Delta\vartheta_{ij}$ . The motion takes place for an arc length equal to $R\,\Delta\varphi_{ij}\,/\,2$, so that points $P'_{ij}$ and $P''_{ij}$

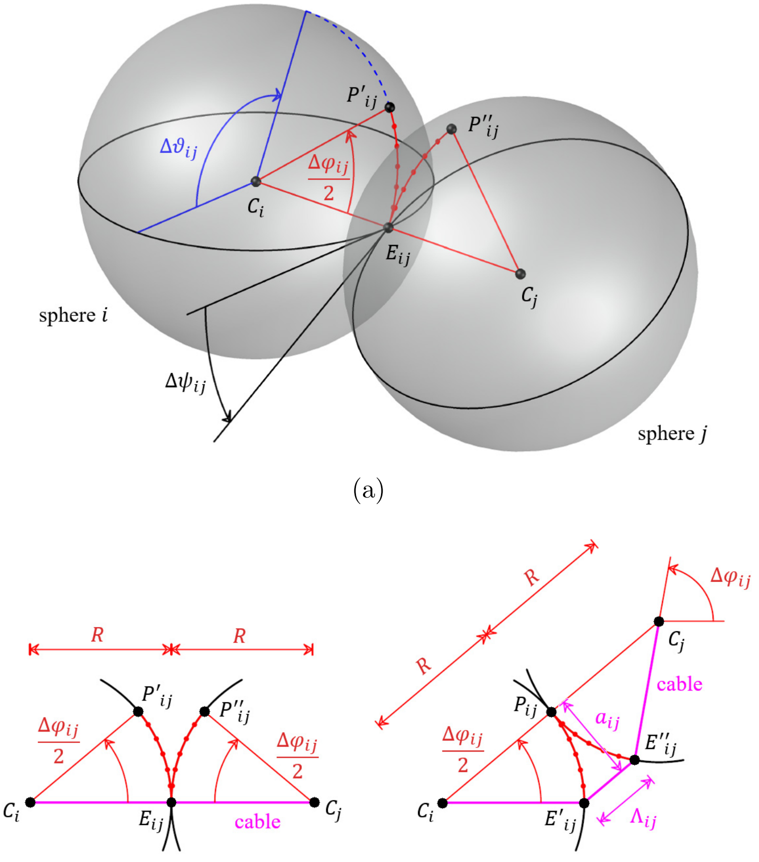

(a)

(b)

(c)

Figure 6: Kinematics of the 3D joint. (a) Degrees of freedom of the spherical contact surfaces: torsion $\Delta\psi_{ij}$, longitude $\Delta\vartheta_{ij}$, and pure rolling along the meridian achieving the relative rotation $\Delta\varphi_{ij}$. (b) Reference (undistorted) state on the slicing plane passing through points $C_i$, $C_j$, $P'_{ij}$ and $P''_{ij}$, and (c) rotated (distorted) state on the same plane, with indication of the cable elongation $\Lambda_{ij}$ and lever arm $a_{ij}$.

are going to coincide in $P_{ij}$. This path is represented by the arcs drawn in red and distinguished by solid dots in Figure 6(a).

Figures 6(b) and 6(c) respectively report a section of the reference undistorted state and the distorted state, obtained with a slicing plane passing through points $C_i$, $C_j$, $P'_{ij}$ and $P''_{ij}$. The motion on this plane is analogous to that of a one-dimensional joint, discussed in Section 2.1. In particular, the cable elongates of the quantity $\Lambda_{ij}$ between the spheres $i$ and $j$, while the distance $a_{ij}$ corresponds to the lever arm of the cable axial force with respect to the pitch point $P_{ij}$ . If $R$ is the radius of the spheres, the expressions for $\Lambda_{ij}$ and $a_{ij}$ are again defined by (2.1a) and (2.1b), respectively.

Observe that the assumed kinematics does not cover all possible configurations of two spheres in pure rolling contact. This is in general a strong non-holonomic constraint: in principle, any two arbitrary points laying on the two spherical surfaces can be brought into contact by following a proper contact path. On the contrary, the motion indicated in Figure 6(a) requires that the arcs of circle $\widehat{E_{ij}P'_{ij}}$ and $\widehat{E_{ij}P''_{ij}}$ have the same length, a property that is not satisfied by all rolling motions. This simplification is such that the relative position of the spheres is completely determined by the angles $\Delta\psi_{ij}$ , $\Delta\vartheta_{ij}$ and $\Delta\varphi_{ij}$ , which can thus be considered as generalized coordinates to describe the configuration of system.

The constraint just described can be directly achieved within the category of flextegrity structures, since it represents the natural three-dimensional extension of the toothed beam joint depicted in Figure 3. The concept is illustrated in Figure 7. An exploded view of the disassembled joint is shown in Figure 7(a): the portions of the spheres that remain in contact during movements associated with a limit admissible value for the angle $\Delta\varphi_{ij}$ , are grooved according to toothed contact profiles, axially symmetrical with respect to the axis of the prestressing tendon. The conjugate profiles are shaped in such a way that relative rotation between the bodies achieves a pure rolling motion along two meridians. A side view of the sections of the two bodies, obtained by cutting them with a plane passing through the contact meridians, is represented in Figures 7(b) and 7(c) for the undistorted reference state and the rotated state, respectively.

This joint corresponds to a pin coupling for the spinning around cable axis (rotation $\Delta\psi_{ij}$ is unconstrained). The contact meridians are defined by the angle $\Delta\vartheta_{ij}$ . The elasticity of the cable and its prestress define the stiffness of the joint against the relative rotation $\Delta\varphi_{ij}$ .

## 3. Physical models

Examples of flextegrity grids, forming two-dimensional structures (plates) and three-dimensional frames (cubes), are now analyzed. Physical prototypes are manufactured via 3D printing to demonstrate the concept of flextegrity lattices.

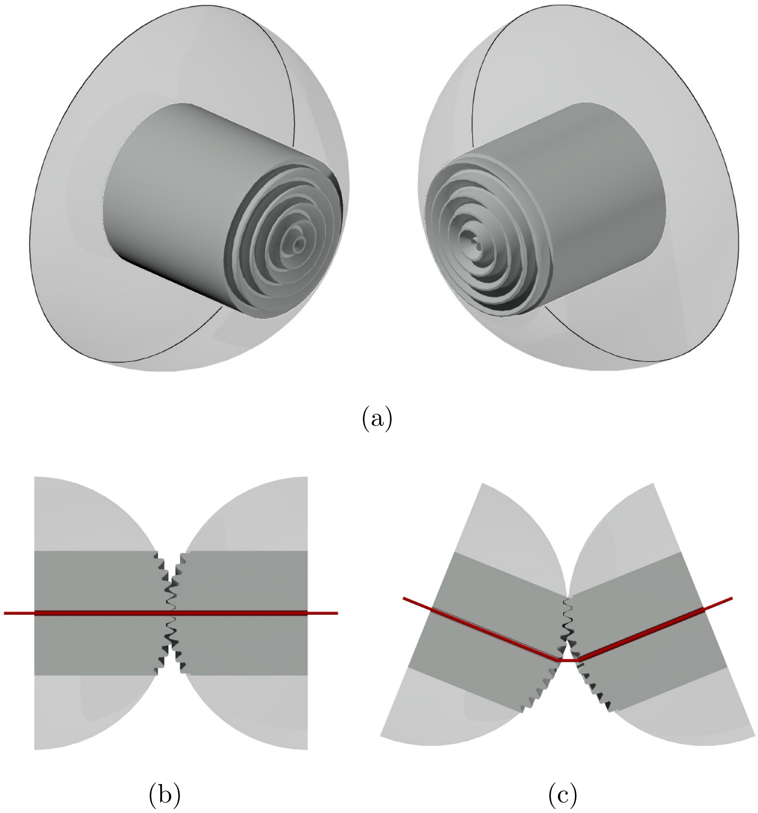

Figure 7: Physical model of the contact joint, with axial-symmetric toothed contact profiles, achieving the kinematic constraint schematized in Figure 6. (a) View of the disassembled joint with the axial-symmetric toothed contact surfaces; longitudinal section of the joint (cable represented by the red solid line) in (b) the reference state and (c) the rotated configuration.

### *3.1. Kinematic analysis of flextegrity plates*

Figure 8 shows two physical models of segmental plates, representative of two-dimensional flextegrity lattices. The assembled basic unit, composed of 4 segments manufactured via 3D printing, is indicated in Figure 8(a), whereas Figure 8(b) shows the corresponding exploded view. The contact surfaces, which correspond to spherical pitch surfaces of radius $R = 30\,\text{mm}$, are shaped according to toothed gears, axial symmetric with respect to axis of the tendons, made with two couples of black-colored parallel elastic rods visible in Figure 8(a). The size of the segments is such that the distance between the pitch surfaces and the center of the segments, defined as the point

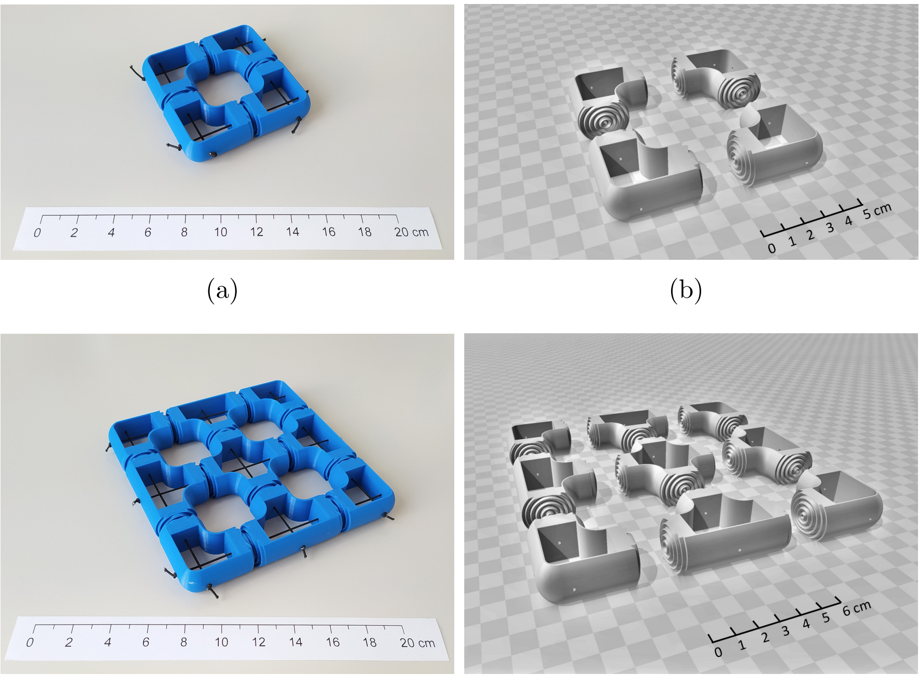

(a) (b) (c) (d)

Figure 8: Segmental plates with flextegrity skeleton. (a) Photograph of the manufactured basic unit composed of 4 segments, and (b) corresponding exploded view. (c) Photograph of a larger plate with 9 segments (4 basic units) and (d) corresponding exploded view. Tendons are black-colored elastic strings.

of intersection of two orthogonal tendons passing through them, is equal to $R$, so that the system reproduces the assembly of a plane of spheres in contact. Figures 8(c) and 8(d) are the counterpart of the previous ones for a larger assembly, made of 4 basic units coupled together, with 9 segments in total. The tendons are elastic strings of diameter 1.2 mm, with axial stiffness equal to $K = 0.058\,\text{N/mm}$ for the prototype of Figure 8(a) and $K = 0.029\,\text{N/mm}$ for the case of Figure 8(c). The difference is due to the fact that the length of the cables of the first prototype is one-half of the second one. The cables are equally prestressed (modulo tolerances) by $N_0 \simeq 1.2\,\text{N}$.

Supposing that the angles of rotation are infinitesimal of the first order (linearized kinematics), the contact joints can be approximated by spherical (spring) hinges, as discussed in Section 2. The physical model of Figure 8(a) is thus schematized as in Figure 9(a), which represents the assembly of 4

L-shaped bars connected by hinges, numbered counterclockwise. One can assume, as degrees of freedom, the absolute rotations of each segment $\alpha_h$, $\beta_h$ and $\gamma_h$, for $h = 1 \ldots 4$, defined by the triad of Figure 9(a). The corner of element 4 is clamped to rule out rigid-body displacements.

The kinematic matrix $\boldsymbol{C}$ for such a structural system can be written as

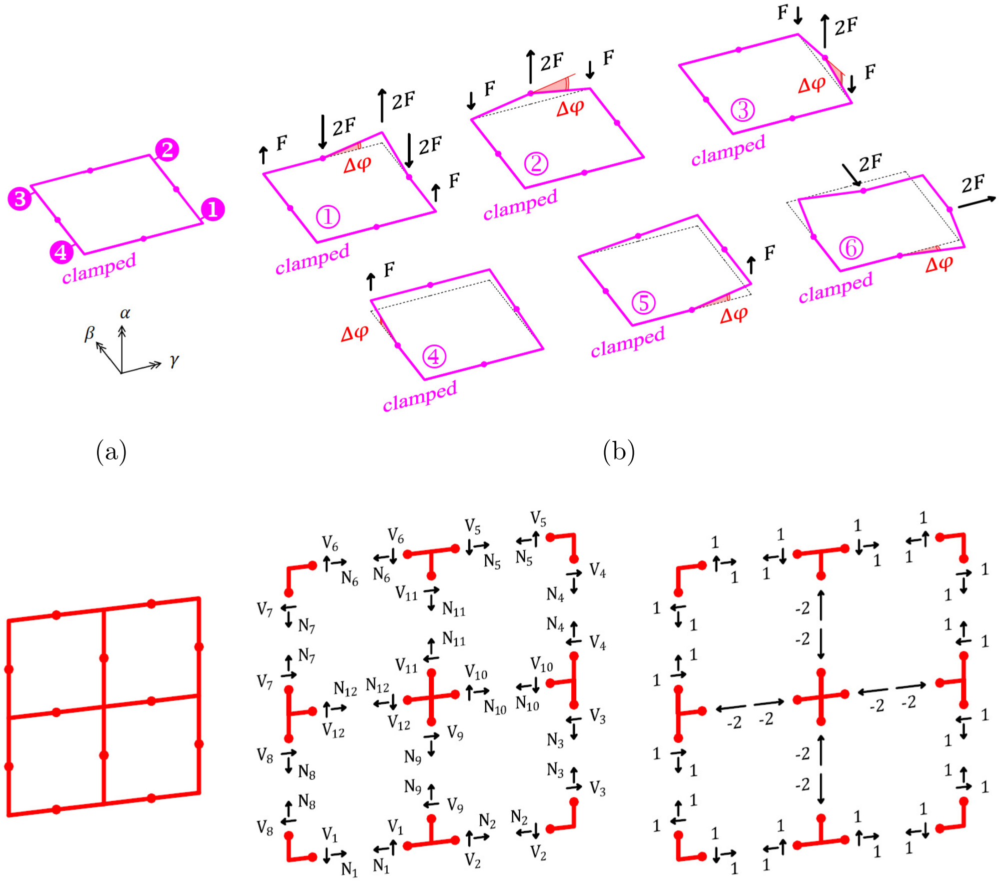

(a) (b)

(c) (d)

Figure 9: Infinitesimal mobility of the plate and states of self-stress. (a) Equivalent chain of pinned L-shaped bars (element 4 is clamped), representative of the basic unit of Figure 8(a), and (b) corresponding six independent mechanisms, with indication of possible systems of external loads to achieve them. (c) Equivalent scheme with pin joints for the larger structure of Figure 8(c), with indication of in-plane internal actions at joints and (d) corresponding state of self-stress.

$$\boldsymbol{C} = \begin{bmatrix} -1 & 0 & 0 & -1 & 0 & 0 & 1 & 0 & 0 & 0 & 0 & 0 \\ 1 & 0 & 0 & -1 & 0 & 0 & -1 & 0 & 0 & 0 & 0 & 0 \\ 0 & -1 & 1 & 0 & 1 & 1 & 0 & 1 & -1 & 0 & 0 & 0 \\ 0 & 0 & 0 & 0 & 0 & 0 & 0 & 0 & 0 & 1 & 0 & 0 \\ 0 & 0 & 0 & 0 & 0 & 0 & 0 & 0 & 0 & 0 & 1 & 0 \\ 0 & 0 & 0 & 0 & 0 & 0 & 0 & 0 & 0 & 0 & 0 & 1 \end{bmatrix} , \tag{3.1}$$

being the degrees of freedom ordered in the array $\mathbf{d}$ defined as

$$\mathbf{d}^T = \left\{ \alpha_1 \quad \beta_1 \quad \gamma_1 \quad \alpha_2 \quad \beta_2 \quad \gamma_2 \quad \alpha_3 \quad \beta_3 \quad \gamma_3 \quad \alpha_4 \quad \beta_4 \quad \gamma_4 \right\} . \tag{3.2}$$

The kinematic matrix (3.1) is rank deficient with respect to the number of degrees of freedom. There are 6 independent mechanisms, associated with the non-trivial solutions of $\boldsymbol{C}\,\mathbf{d} = \mathbf{0}$, which are shown in Figure 9(b). Since the pre-tension of the cable renders the contact joints equivalent to spring hinges, the aforementioned mechanisms can be obtained with the external loads, reported in the same figure. Here, $F = k_\varphi \, \Delta\varphi \, / \, R$, where the angle $\Delta\varphi$ defines the deformation. Observe that the mechanisms of Figure 9(b) corresponds to infinitesimal mobility, but they can be achieved also with finite rotations, with the only exception of mechanism (1). This is not allowed by the actual geometry of the joint, as it is incompatible with the rolling motion of the contact surfaces along meridians, as detailed in Section 2.2.

The plate of Figure 8(a) cannot accommodate any other state of self-stress but the pre-compression introduced by the cables. This is not the case of the larger structure of Figure 8(c). Consider the corresponding pinned-joint assembly, composed of 4 L-shaped, 4 T-shaped and 1 X-shaped bars connected by hinges. This is shown in Figure 9(c) together with the relevant in-plane internal actions. The static unknowns are 36, while the rank of the static matrix $\boldsymbol{S}$, collecting the static equilibrium equations, is equal to 35. This means that it is possible one state of self-stress, schematically shown in Figure 8(d). This could be obtained, e.g., by providing to the central X-shaped segment a positive thermal variation, causing its expansion.

In practical terms, this state of self-stress could be used to reduce the number of prestressing cables, as the two tendons passing through the inner segment are no longer needed to keep the segments in contact. On the other hand, the state of self-stress is not stable, and it can be lost by means of out-of-plane deflections of the plate.

### 3.2. Kinematic analysis of flextegrity cubes

Figure 10 shows two 3D-printed prototypes of flextegrity cubes. The basic unit is displayed in Figure 10(a) and it is now composed of 8 segments, kept together by 12 tendons. The exploded view is shown in Figure 10(b). Figures 10(c) and 10(d) refer to a larger system of 27 segments, formed by the assembly of 8 basic units, coupled by 27 tendons. The contact conjugate profiles are shaped similarly to the two-dimensional case of Section 3.1, forming spherical pitch surfaces of radius $R = 30\,\mathrm{mm}$. In this way, one aims at reproducing a set of spheres in pure rolling contact whose centers follows a SC lattice. Each tendon is again an elastic thread of diameter 1.2 mm, with axial stiffness equal to $K = 0.058\,\mathrm{N/mm}$ for the prototype of Figure 10(a) and $K = 0.029\,\mathrm{N/mm}$ for the prototype of Figure 10(c), due to the different cable lengths. Again, the cables are equally prestressed at $N_0 \simeq 1.2\,\mathrm{N}$.

As done in the previous Section 3.1, independent mechanisms can be caught from the equivalence between the flextegrity assembly and an assembly of hinged beams under the hypothesis of infinitesimal mobility. Figure 11(a) collects the six independent mechanisms, obtained for the basic cubic unit of Figure 10(a). For each mechanism, a possible set of external loads is also indicated, with $F = k_\varphi \, \Delta\varphi \,/\, R$, where $k_\varphi$ is the stiffness of the spring hinges, defined in Section 2.1. All these mechanisms are also allowed in large deflections for the geometry at hand, corresponding to spherical contacts.

For the larger cube of Figure 10(c), nine states of self-stress are possible. These corresponds to the state of self-stress already found for the two-dimensional case of Figure 8(c), which can be now achieved in each planar face and intermediate symmetry plane of the cubic assembly, as shown in Figure 11(b). The major difference, with respect to the case of plates, is that now each state of self-stress is stable, thanks to the confinement of the cubic lattice, which avoid out-of-plane deformations.

The structure of Figure 10(c) may represent a mesoscopic model for a crystalline lattice with strong asymmetry between the responses under tension and compression. Remarkably, the particular form of the eigenstress states could provide an insight about the strategy of crystalline growth in thin films, or the way through which the molecular skeleton could be strengthened via thermal processes or oversized solutes. A certain freedom is maintained for the rotations of sub-elements, which is a peculiar property of flextegrity

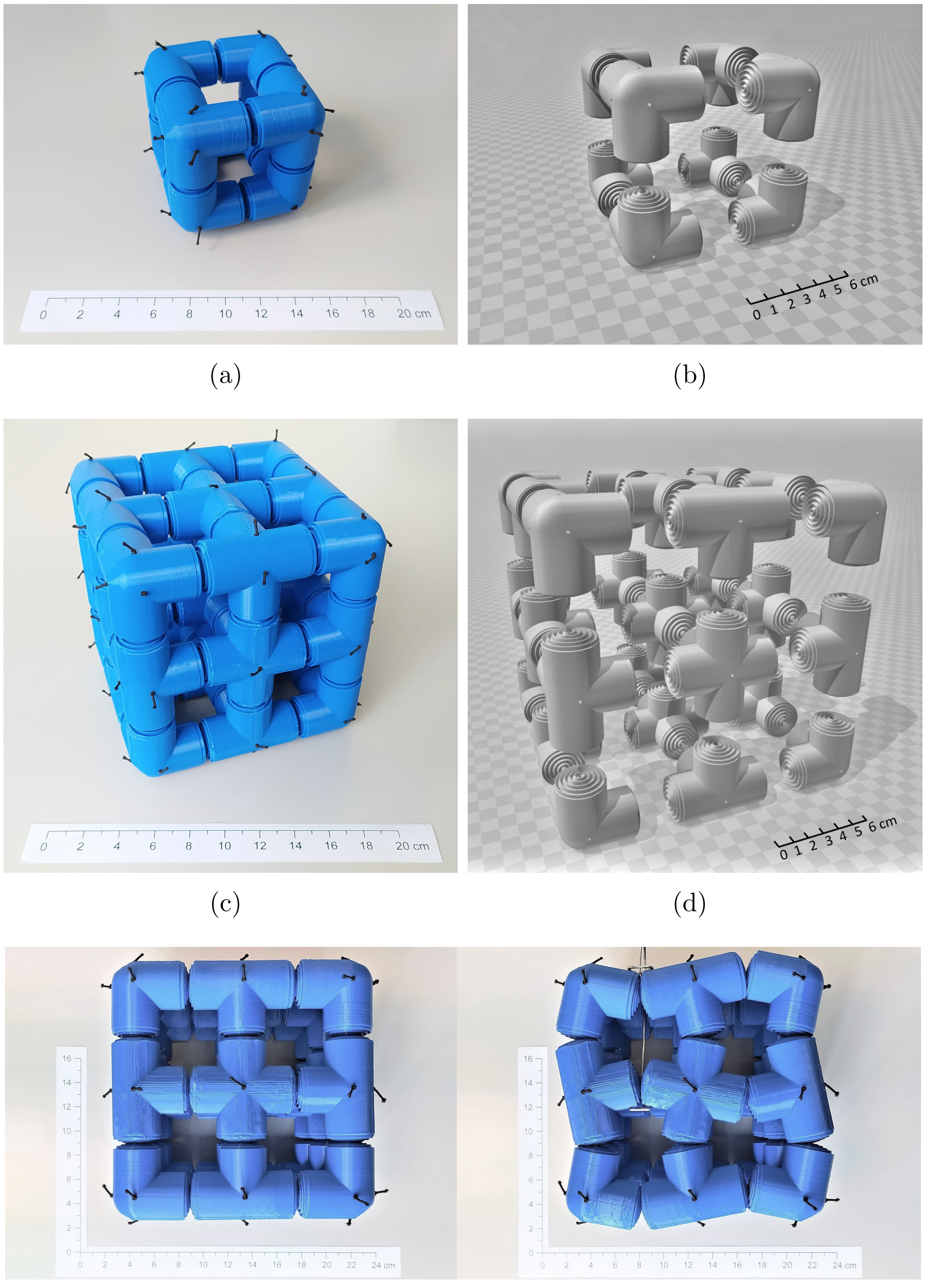

(a) (b)

(c) (d)

(e)

Figure 10: Flextegrity cubes. (a) Photograph of the manufactured basic unit composed of 8 segments and 12 tendons (black-colored elastic strings); (b) corresponding exploded view. (c) Photograph of a larger cube with 27 segments (8 basic units) and 27 tendons; (d) corresponding exploded view; (e) mobility of each face of the cube.

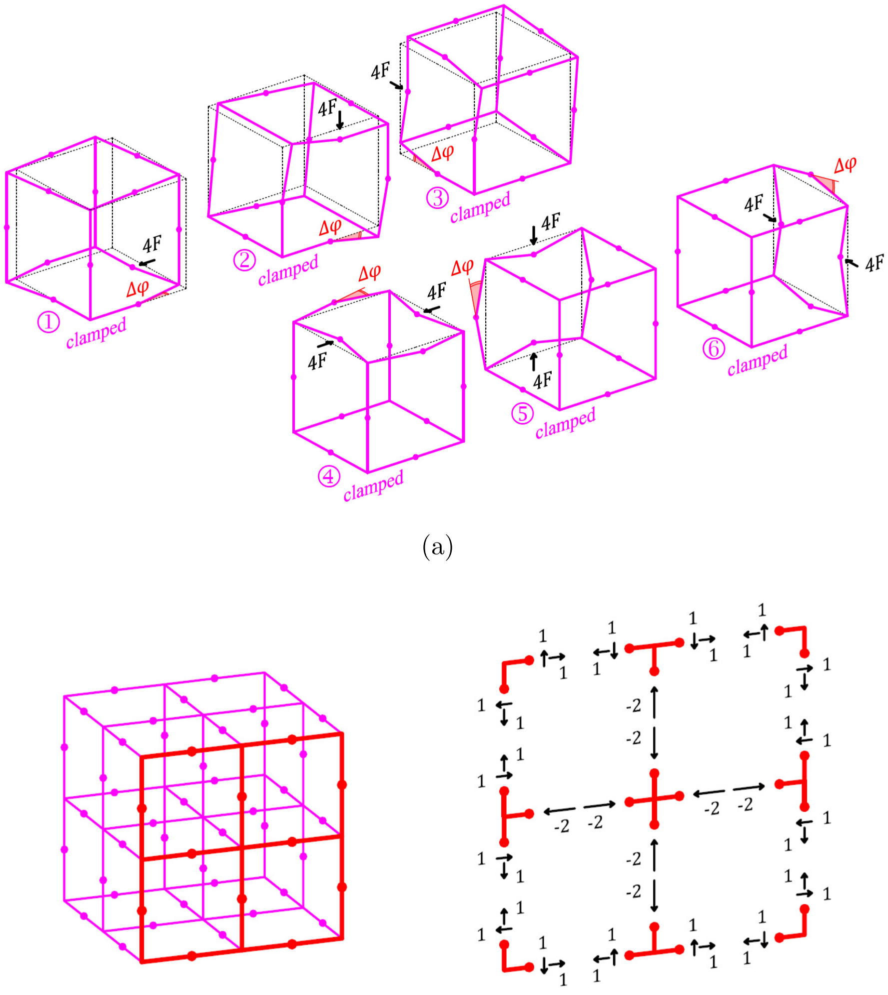

(a)

(b)

Figure 11: Infinitesimal mobility of the segmental cube and states of self-stress. (a) The six independent mechanisms for the cubic basic unit of Figure 10(a), with indication of possible systems of external loads to achieve the mechanisms. (b) Equivalent scheme with pin joints for the larger cube of Figure 10(c), with indication of one of the 9 possible states of self-stress.

lattices. For example, the comparison of Figure 10(e) with Figure 1(b) recalls the molecular re-organization of the scandium fluoride lattice consequent to heating. If the segments were circumscribed by a surface different from a sphere (e.g., an ellipsoid), a deformation of this type could also be associated with a thermal differential expansion of the central segments with respect to the neighboring ones, where the rotation renders the elongation compatible.

### *3.3. Examples of finite deformation*

The kinematic analysis under large rotations presents no conceptual difficulty, but requires a robust numerical approach. An example, instructive for its simplicity, is represented by the out-of-plane bending of flextegrity plates under conservative external forces, such as self-weight. Since in the manufactured prototypes the deformation of the segments is negligible, the strain energy is associated only with the tendons.

Let $H$ indicate the total number of tendons, e.g., $H = 6$ for the case of Figure 8(c). Let $\Delta\boldsymbol{\psi}$, $\Delta\boldsymbol{\vartheta}$ and $\Delta\boldsymbol{\varphi}$ denote the arrays respectively containing all the rotations $\Delta\psi_{ij}$ , $\Delta\vartheta_{ij}$ , and $\Delta\varphi_{ij}$ , as indicated in Section 2.2. With the notation of Figure 6, the increase of strain energy $\Delta U$ when the segments (spheres) roll on each another, starting from the reference state with straight tendons, can be written as

$$\begin{aligned}\Delta U &= \sum_{h=1}^{H} N_{0,h}\,\Lambda_h + \frac{1}{2}\sum_{h=1}^{H} K_h\,{\Lambda_h}^2 \\ &= \sum_{h=1}^{H} N_{0,h}\Big(\textstyle\sum_{i,j}\,\Lambda_{ij}\Big)_h + \frac{1}{2}\sum_{h=1}^{H} K_h\Big(\textstyle\sum_{i,j}\,\Lambda_{ij}\Big)_h^2 .\end{aligned} \tag{3.3}$$

Here, $N_{0,h}$ $(h = 1, \dots, H)$ represents the initial prestress of the $h-$th tendon, $K_h$ its axial stiffness, whereas $\Lambda_h$ denotes its total elongation, which is the sum of the contributions $\Lambda_{ij}$ (detailed in Figure 6(c)) due to the relative rotation of the two spheres $i$ and $j$ in contact, through which the $h-$th cable passes. Since $\Lambda_{ij}$ is a function of $\Delta\varphi_{ij}$ , the strain energy $\Delta U$ results to be a function of $\Delta\boldsymbol{\varphi}$.

The work $\Delta W$ of the external conservative loads $F_s$ , for $s = 1, \dots, S$, applied orthogonally to the initially-planar (mid) surface of the plate at $S$ points, depends upon the out-of-plane displacements $w_s$ of these points, i.e.,

$$\Delta W = \sum_{s=1}^{S} F_s\,w_s\,. \tag{3.4}$$

Observe that the displacements $w_s$ depend on the position of the segments (spheres) in the distorted state, which is defined by the rotations $\Delta\psi_{ij}$ , $\Delta\vartheta_{ij}$ , and $\Delta\varphi_{ij}$ . Hence, $\Delta W$ is a function of the vectors $\Delta\boldsymbol{\psi}$, $\Delta\boldsymbol{\vartheta}$ and $\Delta\boldsymbol{\varphi}$.

The equilibrium condition is defined by

$$\Delta U - \Delta W = \Delta U(\Delta\boldsymbol{\varphi}) - \Delta W(\Delta\boldsymbol{\psi}, \Delta\boldsymbol{\vartheta}, \Delta\boldsymbol{\varphi}) = \min\,, \tag{3.5}$$

under the constraints introduced, besides the boundary conditions, by the kinematic skeleton. The latter correspond to the kinematic conditions that each ring of the grid, following the path of segments in contact, must be a closed loop: starting from one segment, one shall recover the same position after the composition of displacements dictated by rotations $\Delta\psi_{ij}$ , $\Delta\vartheta_{ij}$ , and $\Delta\varphi_{ij}$ at each pair of consecutive segments.

The 3D-printed plate first considered consists in the assembly of 2 basic units (6 segments), of the type indicated in Figure 8(a), now coupled in series. The kinematic skeleton is that of 6 spheres of radius $R = 30\,\mathrm{mm}$ in mutual contact, arranged as in Figure 12(a). The tendons parallel to the short sides are characterized by axial stiffness equal to $K_h = 0.058\,\mathrm{N/mm}$ and they have been pre-tensioned at $N_{0,h} \simeq 1.7\,\mathrm{N}$ ($h = 1, 2, 3$), while for those following the long sides one has $K_h = 0.029\,\mathrm{N/mm}$ and $N_{0,h} \simeq 1.4\,\mathrm{N}$ ($h = 4, 5$).

The test of Figure 12 was preliminary carried out. As indicated in Figure 12(a), the structure is clamped at one of the short sides and it is subjected to the forces $F_1 = F_2 = 0.1\,\mathrm{N}$, applied at the opposite sides. The tested plate is placed vertically, in such a way that the planar face of the undeformed plate is parallel to the gravity field, acting along the direction of the short sides: this allows to disregard the action of the self-weight. The symmetry of the problem is such that the structure deform as a one-dimensional beam, for which an analytic solution can be found [19]. This served to validate the numerical computations, which used the Nelder-Mead algorithm [25], implemented in Mathematica® for energy minimization. Figures 12(b) and 12(d) show different views of the deformation of the prototype, which are juxtaposed to the deformed shapes obtained via calculation, reproduced with a CAD tool and reported in Figures 12(c) and 12(e), respectively.

Analytical and numerical solutions qualitatively coincide. A quantitative comparison is reported in Table 1, in terms of the out-of-plane displacement $w_{\mathrm{A}}$ of the reference point A indicated in Figure 12. It should be mentioned that there are potential sources of inaccuracy: precision of measurement with a dynamometer and ruler, 3D printing tolerances, parasitic frictional forces

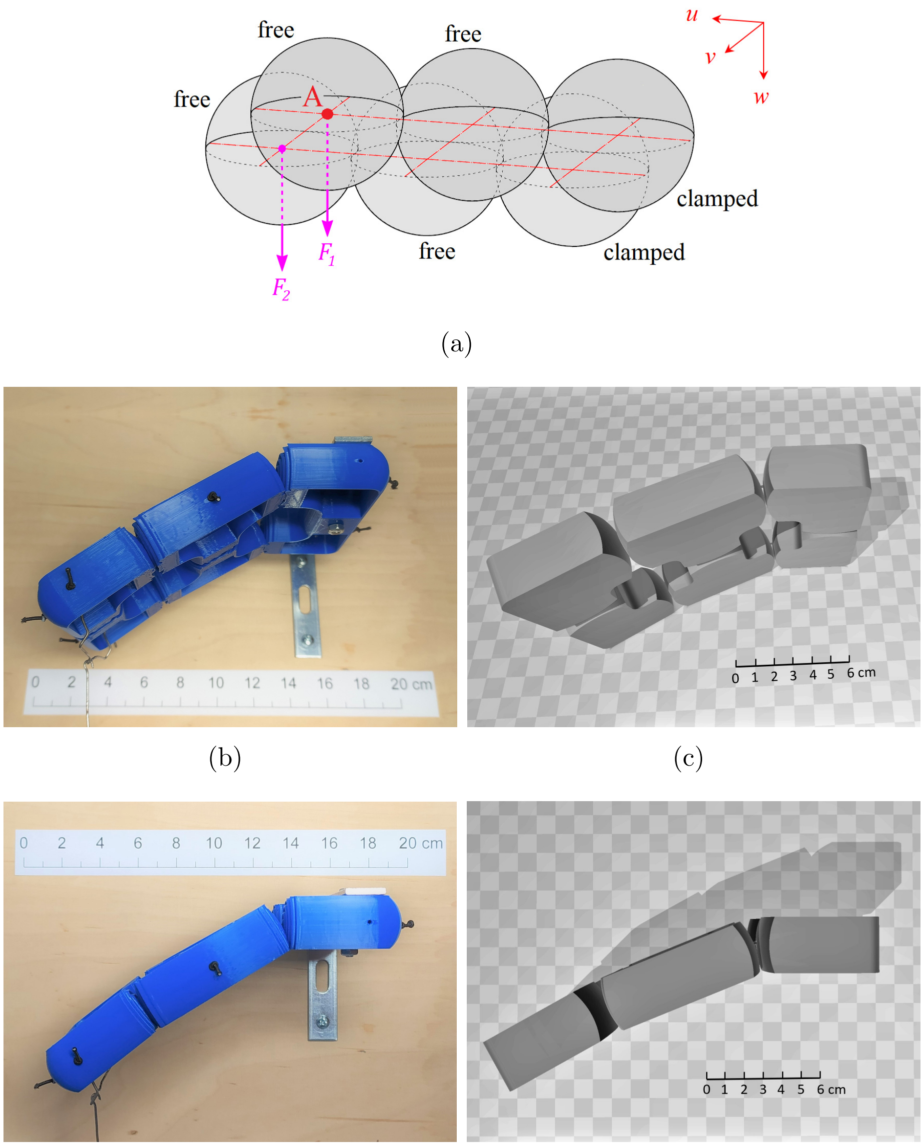

(a)

(b) (c)

(d) (e)

Figure 12: Flextegrity plate composed of 6 segments (two basic units of Figure 8(a)) under symmetric external loads. (a) Schematics of the spherical contact profiles with indication of the constraints, the points of application of the loads, and the reference point A; (b) and (d) are views of the deformed shape for the manufactured prototype, while (c) and (e) are the corresponding views of shapes calculated from the model.

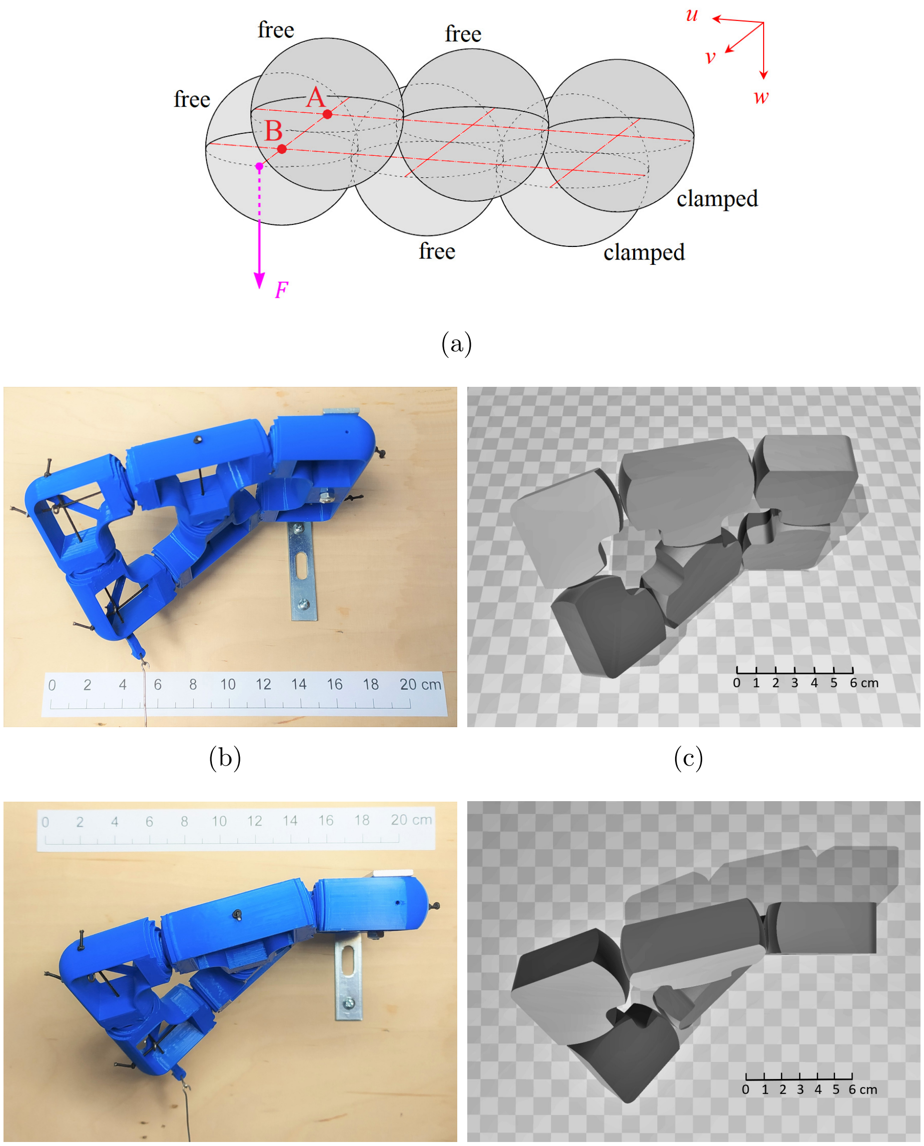

(a)

(b) (c)

(d) (e)

Figure 13: Flextegrity plate composed of 6 segments (two basic units of Figure 8(a)) under eccentric external load. (a) Schematic of the spherical contact profiles with indication of the constraints, the point of application of the load, and the reference points A and B. (b) and (d) are different views of the deformed shape for the manufactured prototype, while (c) and (e) are the corresponding views of shapes calculated from the model.

Table 1: Comparison between the deflection of the physical prototypes and that predicted by the model, in terms of the out-of-plane displacements $w_\mathrm{A}$ and $w_\mathrm{B}$ of the reference points A and B, indicated in Figures 12, 13 and 14.

| Load case | Figure | Point | Experiment | Model |
|---|---|---|---|---|
| symmetric forces | 12 | A | $44 \pm 2\,\mathrm{mm}$ | $37 \pm 5\,\mathrm{mm}$ |
| eccentric force | 13 | A | $27 \pm 2\,\mathrm{mm}$ | $23 \pm 5\,\mathrm{mm}$ |
| | | B | $63 \pm 2\,\mathrm{mm}$ | $64 \pm 5\,\mathrm{mm}$ |
| self-weight | 14 | A | $26 \pm 2\,\mathrm{mm}$ | $25 \pm 5\,\mathrm{mm}$ |

at the joints. In particular, the uncertainty results from the measurement errors that affect the initial data of the problem, specifically for what concerns $N_{0,h}$, $K_h$ and $F_1 = F_2$, which can affect the theoretical calculations. That said, the agreement between theory and experiment is reputed good.

The same physical model was tested under the eccentric force $F = 0.4\,\mathrm{N}$ indicated Figure 13(a). Figures 13(b)-13(d) and Figures 13(c)-13(e) again compare the observed deflection with that obtained via numerical calculations. The flexural-torsional deformation is correctly reproduced by the model. The quantitative comparison of the out-of-plane deflections $w_\mathrm{A}$ and $w_\mathrm{B}$ of the reference points A and B, indicated in Figure 13, is again reported in Table 1. Taking into account the potential sources of error, the model provides accurate results with respect to the measured displacements of the prototype.

The last test regards the square 3D-printed plate of Figure 8(c), placed horizontally in the (vertical) gravity field. This is composed of 9 segments (4 basic units), and it is supported at the mid central segment and subjected to self-weight. The pitch surface radius is again $R = 30\,\mathrm{mm}$, and the tendons, whose axial stiffness is $K_h = 0.029\,\mathrm{N/mm}$ for $h = 1, \dots, 6$, are pre-tensioned by $N_{0,h} = 1.2\,\mathrm{N}$. The loads $F_s \simeq 0.1\,\mathrm{N}$ represent the self-weight of each segment. Figure 14 collects two different views for the plate in the deformed state, and compares them with the corresponding shapes, obtained via calculations. The deformation recalls the shape of a hyperbolic paraboloid, which is perfectly caught by the model. The vertical displacement $w_\mathrm{A}$ of the reference point A, indicated in Figure 14(c), which corresponds to the center of the corner sphere, is again reported in Table 1 to compare experiment and theory. The agreement, in this case, is excellent.

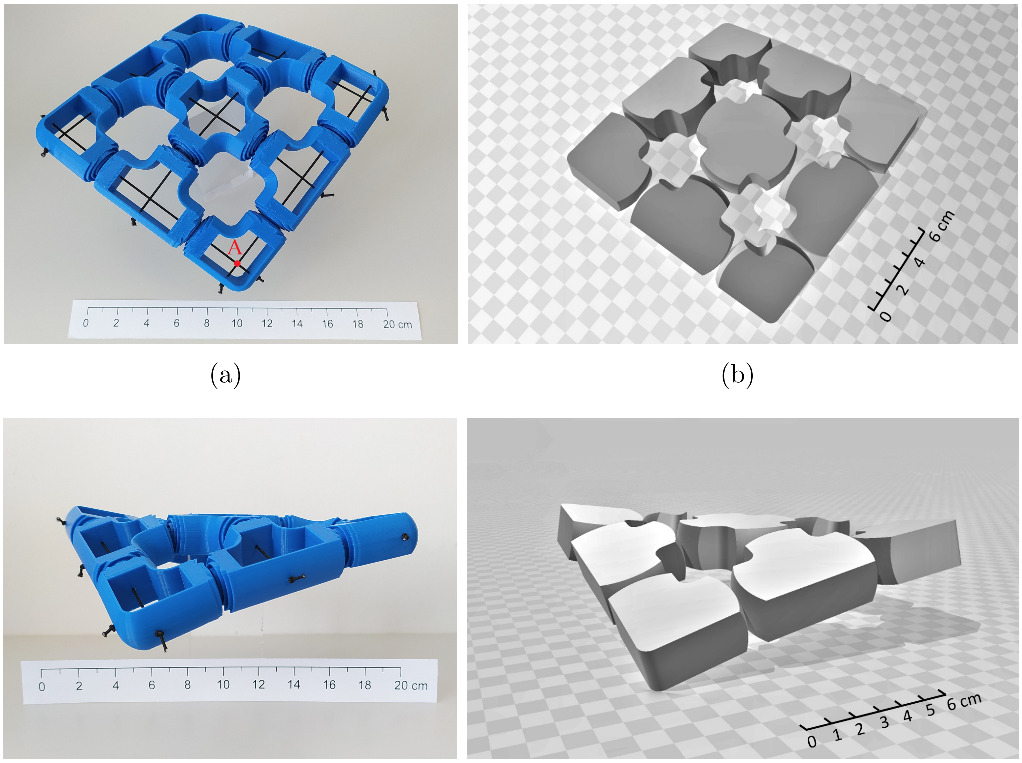

(a) (b)

(c) (d)

Figure 14: Deformation of a flextegrity plate composed of 9 segments (4 basic units), under self-weight and supported at the middle. (a),(c) Different views of the deformed shape for the manufactured prototype, with indication of the reference point A, and (b),(d) corresponding views for the shape obtained via computation.

In conclusion, taking into account the uncertainties in the physical model, in terms of measured tensile force and stiffness of the tendons, effects of parasitic friction at the contact joints and with the cables, possible inaccuracy in the application of external loads, and 3D-printing tolerances, the agreement between theory and experiments is considered more than satisfactory, both qualitatively and quantitatively.

## 4. Discussion

Flextegrity lattices, mimicking an assembly of rolling spheres, can represent the basis for mesoscopic models of crystalline microstructures, where the molecular rotations are non-negligible degrees of freedom. Similarly, the mesoscopic model can represent the actual microstructure of metamaterials, with mechanical properties dictated by the kinematic skeleton. However, the conceptual model can be declined in many other forms. In fact, by varying the tendon stiffness/prestress, as well as the shape of the pitch surfaces of the contact joints, with geometries departing from the spherical paradigm (paraboloids, ellipsoids or more complex surfaces), a wide range of different in-type responses could be attained. As discussed in [19, 20] for beam-like structures, the stiffness and prestress of the tendons affects the equivalent elasticity of the lattice; on the other hand, the shape of the pitch surfaces dictates the cable elongation $\Lambda_{ij}$ and the lever arm $a_{ij}$ at each joint, thus modifying the form of constitutive relations.

The assemblies so far considered are, in practice, SC lattices of spheres with the same radius $R$ in pure rolling contact, but this is just one particular category. Figure 15(a) reports a plan view of a lattice made with spheres of two different sizes, connected by tendons represented in magenta color. Figure 15(b) indicates that the system permits the relative rotation of the spheres, with a motion similar to that already observed in Figure 5(c). Note, however, that also a shear-like deformation, following the scheme of Figure 15(c), can be achieved with such a new arrangement. On the contrary, a motion of this type is prevented in the assembly of equal spheres by the constraint of pure rolling contact, as discussed in Figure 5(d).

Spherical segments of equal size could also be arranged in the form of (nano-)tube lattices. Figure 16(a) schematically represents a tube formed

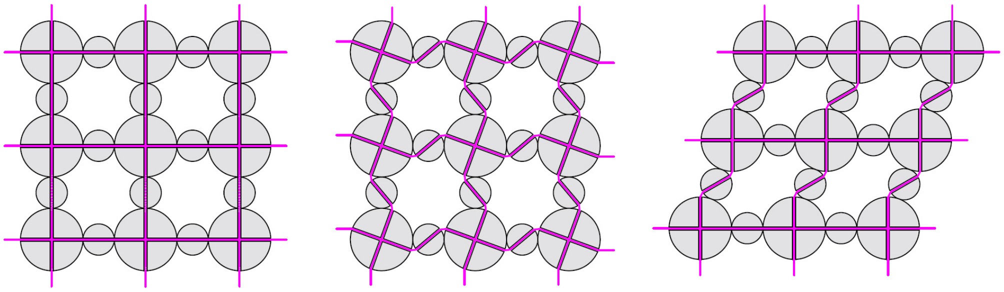

(a) (b) (c)

Figure 15: Lattices made with spherical segments with diverse radius. (a) Schematics of the arrangement (tendons represented by magenta lines), which allows for both (b) relative rotations and (c) shear-like deformation between the sub-particles.

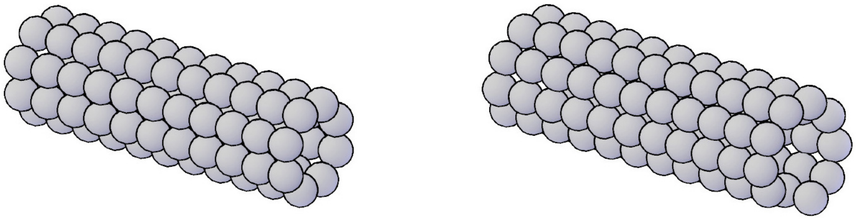

(a) (b)

Figure 16: Two possible arrangements for (nano-)tube lattices. Arrangement with (a) parallel rings and (b) helically wound chains.

by parallel rings of spheres. In this case the integrity is granted by straight longitudinal tendons, as well as by circular tendons that hoop the rings. Another possible configuration follows the helical arrangement of Figure 16(b). Apart from straight tendons parallel to the axis of the tube, here the segments are kept in contact by tendons that follow the helix defined by the sphere centers.

In a recent article [21], the authors have shown that the contact joints of a segmental beam can achieve multiple equilibrium states (non-convex energy) when the mobility of the tendon is increased by enlarging the segmental cavities. The possible extension of this concept to flextegrity lattices is shown in Figure 17. The multi-stable behavior is obtained by shaping the internal cavity hollowed inside the segments, as indicated in Figure 17(a), so that the pivot point of the cable (exit point from the tubular sheath) is set back with respect to the pitch profile. This is formed, as discussed in [21] for the one-dimensional case, by three smoothly-connected arcs of circle with radii $R$ and $2R$. The joint is multi-stable, because the are more than one configurations associated with the minimal length of the tendon. Two-dimensional structures can be obtained by assembling cross-shaped segments according to the scheme of Figure 17(b): this “straight” configuration depicts a non-chiral lattice. There are, however, other two “rotated” equilibrium states, as per Figures 17(c) and 17(d), that provide a chiral micro-arrangement, stable under null external actions. This is an example of how a homogeneous assemblage of non-chiral objects can have chirality. The concept could also be extended to three-dimensional multi-stable flextegrity lattices, although the design of joints with a complex 3D mobility certainly requires additional investigation. The possibility of manufacturing a 3D snapping coupling between the seg-

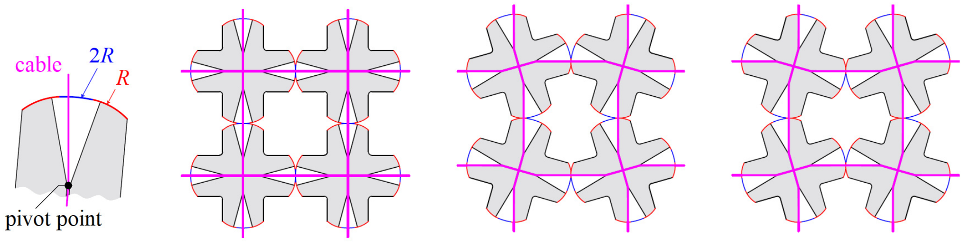

(a) (b) (c) (d)

Figure 17: Other types of flextegrity lattices, with multi-stable contact joints. (a) Schematics of the segmental cavity (blank region), which increases the mobility of the cable inside the segment, and pitch lines consisting of 3 smoothly-connected arcs of circle, as suggested in [21], with radii $R$ and $2R$. Equilibrium configurations under null external actions: (b) "straight" (non-chiral) state and (c),(d) "rotated" (chiral) states.

ments, leveraging the recently proposed variant [22, 26] of flextegrity beams, is yet to be fully investigated.

In all the aforementioned cases, rolling motions rely on the hypothesis that all the segments remain in contact along the pitch surfaces but, in general, some components may detach under tension. Moreover, the hypothesis of rigid segments should be relaxed when the segmental contact is achieved by very stiff and highly pre-tensioned tendons. In this case, the change of shape of the pitch profiles under contact forces will produce a modification of the constitutive equations.

## 5. Conclusions

Flextegrity lattices composed of segments in a simple cubic arrangement, mimicking a compact assembly of spheres in pure rolling contact, have been proposed, theoretically analyzed, prototyped in physical models and tested. Geometric compatibility provides a kinematic skeleton which constrains the energetic landscape, enforcing constitutive properties that are dictated, beside the stiffness and pretension of the tie tendons, by the shape of the pitch surface of the contact joints. The lattice could represent a mesoscopic model for the homogeneous microstructure of a crystal with interacting molecules, whose qualities as a whole depend upon the orientation of the molecules and the mutual forces acting between them. Metamaterials built upon flextegrity frames enjoy particular bulk properties and are amenable of (molecular) vibrations, which suggests their use as resonators.

The static-kinematic analysis has also demonstrated that the lattice can undergo self-equilibrated stress states (eigenstress). This finding could be related to possible strategies for the growth of the crystal by the addition of layer after layers, suggest a way by which contact forces can be increased by inserting molecules with different size into the lattice, or motivate the change in the microstructural orientation in response to the thermal expansions of the molecules. The particular kinematic, supplemented by the consideration of electric charges on the segments, could also represent a mesoscopic model for piezoelectric effects.

The cases analyzed here represent the simplest flextegrity lattices. One can imagine three-dimensional grids composed of segments with diverse geometry, different contact surfaces, possibly amenable of multiple equilibrium states, representing a transition from chiral to non-chiral phases as a consequence of thermal or mechanical stimuli. An improved model could account for the different response of the assembly under tension, compression and bending, by considering the detachment of segments. The dynamics of the lattice, for what concerns either the global response of the whole, or the local vibrations at the segmental (molecular) level, possibly complicated by the fact that multi-stable contact joints may snap in response to localized perturbations, still need to be analyzed. We postpone all these issues to forthcoming works.

**Data accessibility.** This article does not contain any additional data.

**Authors' contribution.** CB and GRC developed the model and the design. CB built and tested the prototypes. Both authors wrote the paper and gave final approval for publication.

**Competing interests.** There are no competing interests to declare.

**Funding.** This research did not receive any specific grant from funding agencies in the public, commercial, or not-for-profit sectors.

## References

[1] W. Thomson, Baltimore Lectures on Molecular Dynamics and the Wave Theory of Light, Clay and Sons, London, 1904.

[2] V. Erofeev, I. Pavlov, Structural modeling of metamaterials, Springer, Cham, CH, 2021.

[3] R. Del Carpio Minaya, Y. Atencio, Applications of spring-mass model on crystalline lattices, in: 2017 XLIII Latin American Computer Conference (CLEI), IEEE, 2017, pp. 1–8.

[4] I. Müller, P. Villaggio, A model for an elastic-plastic body, Archive for Rational Mechanics and Analysis 65 (1) (1977) 25–46.

[5] G. Puglisi, L. Truskinovsky, Mechanics of a discrete chain with bi-stable elements, Journal of the Mechanics and Physics of Solids 48 (1) (2000) 1–27.

[6] A. Askar, A. Cakmak, A structural model of a micropolar continuum, International Journal of Engineering Science 6 (10) (1968) 583–589.

[7] Z. Bažant, M. Christensen, Analogy between micropolar continuum and grid frameworks under initial stress, International Journal of Solids and Structures 8 (3) (1972) 327–346.

[8] A. Aly, A. Mehaney, Low band gap frequencies and multiplexing properties in 1d and 2d mass spring structures, Chinese Physics B 25 (11) (2016) 114301.

[9] M. Lombardo, H. Askes, Elastic wave dispersion in microstructured membranes, Proceedings of the Royal Society A: Mathematical, Physical and Engineering Sciences 466 (2118) (2010) 1789–1807.

[10] B. Afra, M. Nazari, M. Kayhani, A. Delouei, G. Ahmadi, An immersed boundary-lattice boltzmann method combined with a robust lattice spring model for solving flow–structure interaction problems, Applied Mathematical Modelling 55 (2018) 502–521.

[11] A. Santhanam, Modeling, simulation, and visualization of 3d lung dynamics, Ph.D. thesis, School of Electrical Engineering and Computer Science, University of Central Florida, Orlando, Florida, USA (2006).

[12] F. Qin, J. Chen, U. Aydemir, A. Sanson, L. Wang, Z. Pan, J. Xu, C. Sun, Y. Ren, J. Deng, et al., Isotropic zero thermal expansion and local vibrational dynamics in (Sc, Fe) $F_3$, Inorganic chemistry 56 (18) (2017) 10840–10843.

[13] A. Vasiliev, Modeling of micropolar type chiral structures, Letters on Materials 3 (3) (2013) 248–251.

[14] A. Vasiliev, I. Pavlov, Models and parameters of cosserat hexagonal lattices with chiral microstructure, in: IOP Conference Series: Materials Science and Engineering, Vol. 1008, IOP Publishing, 2020, p. 012017.

[15] P. Mora, D. Place, A lattice solid model for the nonlinear dynamics of earthquakes, International Journal of Modern Physics C 4 (06) (1993) 1059–1074.

[16] Y. Wang, P. Mora, Macroscopic elastic properties of regular lattices, Journal of the Mechanics and Physics of Solids 56 (12) (2008) 3459–3474.

[17] S. Sadao, Fuller on tensegrity, International Journal of Space Structures 11 (1-2) (1996) 37–42.

[18] S. Juan, J. Tur, Tensegrity frameworks: static analysis review, Mechanism and Machine Theory 43 (7) (2008) 859–881.

[19] C. Boni, M. Silvestri, G. Royer-Carfagni, Flexural tensegrity of segmental beams, Proceedings of the Royal Society A: Mathematical, Physical and Engineering Sciences 476 (2237) (2020) 20200062.

[20] C. Boni, G. Royer-Carfagni, A nonlocal elastica inspired by flexural tensegrity, International Journal of Engineering Science 158 (2021) 103421.

[21] C. Boni, G. Royer-Carfagni, Equilibrium of bi-stable flexural-tensegrity segmental beams, Journal of the Mechanics and Physics of Solids 152 (2021) 104411.

[22] C. Boni, G. Royer-Carfagni, Energy harnessing in the snap-through motion of a flexural-tensegrity flagellum, Mechanism and Machine Theory 173 (2022) 104845.

[23] H. Kroto, J. Heath, S. O'Brien, R. Curl, R. Smalley, C60: Buckminsterfullerene, nature 318 (6042) (1985) 162–163.

[24] A. Bubenchikov, M. Bubenchikov, D. Mamontov, A. Lun-Fu, Md-simulation of fullerene rotations in molecular crystal fullerite, Crystals 9 (10) (2019) 496.

[25] J. Nelder, R. Mead, A simplex method for function minimization, The computer journal 7 (4) (1965) 308–313.

[26] C. Boni, P. M. Reis, G. Royer-Carfagni, Flexural-tensegrity snapping tails for bio-inspired propulsion in fluids, Extreme Mechanics Letters 56 (2022) 101853.